Determination of pressure and load characteristics of flexible revolving wings by means of tomographic PIV

van de Meerendonk, Remco; Perçin, Mustafa; van Oudheusden, Bas

Publication date
2016

Document Version
Accepted author manuscript

Published in
Proceedings of the International Workshop on Non-Intrusive Optical Flow Diagnostic

Determination of pressure and load characteristics of flexible revolving wings by means of tomographic PIV

Remco van de Meerendonk[1*], Mustafa Percin[1], Bas van Oudheusden[1]
1: Dept. of Aerospace Engineering, Delft University of Technology, the Netherlands
* Correspondent author: remcovandemeerendonk@gmail.com

This study explores the flow field and fluid-dynamic loads generated by revolving low-aspect-ratio wings. The pressure field and load characteristics are successfully reconstructed from the phase-locked tomographic measurements in three independently measured volumes along the span of the wing. The vortical structures encompass a low pressure region and the spatial gradient information of the pressure field provides greater insights in their stability mechanisms. The low pressure region associated with the leading edge vortex and its close position to the wing surface are responsible for the high resultant forces acting on the wing. Simultaneous force measurements show a reasonable agreement with the reconstructed loads. The sectional lift and drag characteristics provide greater insights into the distributed load mechanisms along the span.

INTRODUCTION

Flapping-wing flight is characterized by unsteady three-dimensional effects, where the formation of a stable leading edge vortex (LEV) is one of the most prominent mechanisms responsible for the enhanced aerodynamic forces sustaining flapping flight (Sane, 2003). It has been hypothesized that spanwise pressure gradients, the associated vorticity transport (Ellington et al. 1996) and the apparent rotational accelerations which are characterized by the Rossby number (Lentink & Dickinson 2009, Jardin and David 2014, 2015) play an important in the LEV stability mechanisms. The sustained LEV occurring in a revolving motion is accompanied by a low pressure region at the suction side of the airfoil. The suction forces that act normal to the wing surface are dominant such that for a rigid wing the resultant force vector acts normal to the wing chord for angles of attack higher than 10 deg (Usherwood & Ellington, 2002; Birch, 2004).

Although different studies have indicated the possible benefits of wing flexibility on the aerodynamic performance (Shyy et al., 2010), it is often not taken into account in mechanical model simulations. In terms of spanwise flexural stiffness, Combes & Daniel (2003) found that for biological flyers the spanwise rigidity is 1-2 orders of magnitude higher than the chordwise rigidity.

By incorporating the pressure field in the analysis, the link between the temporal evolution of the vortical structures and the associated pressure forces can be obtained in more detail. This allows to study the stability mechanisms of the LEV in detail and to explain the enhanced aerodynamic forces sustaining flapping flight. The aim of the current study is to investigate the spatial-temporal evolution of the flow field of revolving low-aspect-ratio wings, and to connect the associated vortical structures and pressure fields to the temporal evolution of the fluid-dynamic forces acting on the wing. The experimental campaign consists of phase-locked tomographic particle image velocimetry measurements complemented with simultaneous force measurements. Subsequently, from the velocity data the pressure fields are reconstructed as well as the loads acting on the wing.

EXPERIMENTAL METHODOLOGY

Three different chordwise flexible wings were tested in order to investigate the influence of wing flexibility: a rigid wing from 1 mm thick Plexiglass, a moderately flexible wing from 175 μm PET and a highly flexible wing from 125 μm PET. Each wing has an angle of attack of 45 deg in their undeformed condition and an aspect ratio of 2. The Reynolds number is 10,000 (based on a chord length c of 50 mm) and the Rossby number is 1.93.

The 75% span position of the wing model is taken as the reference position to characterize the motion kinematics. The non-dimensional travel length is given in terms of chords travelled ($\delta^* = \delta/c$, where δ is the distance travelled by the wing at the reference spanwise position). The revolving wing motion starts from rest and is subjected to a constant acceleration to reach a terminal velocity V_t of 0.2 m/s over a time interval corresponding to a displacement of one chord length (i.e. $0 < \delta^* < 1$), after which the wing continues to revolve at a constant velocity (i.e. for $\delta^* > 1$). The temporal resolution ($TR^* = TR \cdot V_t/c$) is the time between the phases.

Phase-locked tomographic PIV measurements were performed in three volumes along the wing span for selected phases of the revolving motion as given in Figure 1.

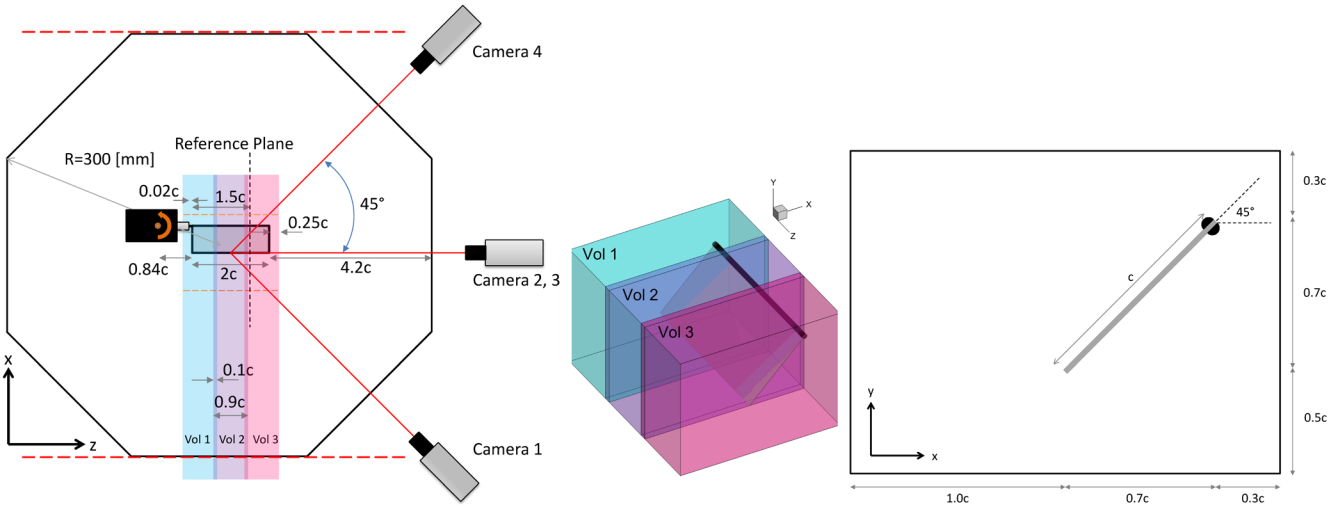

Fig. 1 *Left*: Schematic top view and experimental setup. *Middle*: Schematic of the measurement volumes. *Right*: Schematic representation of the chordwise field of view. Schematics illustrated with a rigid wing.

The flow fields obtained in the PIV measurements are defined in the inertial "laboratory" reference frame. The velocity field data is converted from the inertial reference frame to the rotating reference frame as,

$$\mathbf{u}_{\text{rotating}} = \mathbf{u}_{\text{inertial}} - \Omega \times \mathbf{r}_{\text{pv}} \qquad (1)$$

where $\mathbf{u}$ is the velocity vector, Ω the angular velocity of the wing and $\mathbf{r}_{\text{pv}}$ the position vector measured from the rotation axis. In the remainder of this section the considered velocity is the apparent velocity in the rotating reference frame. Assuming incompressible flow, a constant viscosity and discarding gravity, the pressure gradients in the rotating reference frame are evaluated as,

$$\frac{1}{\rho}\nabla p = -\frac{D\mathbf{u}}{Dt} - \underbrace{\boldsymbol{\Omega} \times (\boldsymbol{\Omega} \times \mathbf{r}_{\text{pv}})}_{\text{Centrifugal}} - \underbrace{2\ \boldsymbol{\Omega} \times \mathbf{u}}_{\text{Coriolis}} - \underbrace{\frac{d\boldsymbol{\Omega}}{dt} \times \mathbf{r}_{\text{pv}}}_{\text{Euler}} + \nu\nabla^2\mathbf{u} \qquad (2)$$

where p is the pressure and v is the kinematic viscosity. The centrifugal, Coriolis and Euler effects introduce apparent forces due to working in a non-inertial reference frame. The material derivative $D\mathbf{u}/Dt$ is calculated according to the Eulerian approach, by separately evaluating the local time-derivative and convective terms. Subsequently the pressure gradient field is integrated by setting up a Poisson problem as,

$$\nabla^2 p = \nabla \cdot (\nabla p) \qquad (3)$$

The 3D Poisson problem is discretized using a finite second-order-accurate central-difference scheme. At the boundaries of the integration domain Neumann boundary conditions (spatial gradient of pressure) normal to the boundary are imposed. The Neumann boundary conditions are set up using a second order accurate central difference scheme by introducing ghost points outside of the calculation domain. By means of a mask convergence study, the optimum mask size, defined as the smallest size for which converged lift and drag are obtained, was determined to be 7 vectors.

The fluid-dynamic loads are reconstructed by evaluating the integral momentum balance obtained by integrating the Navier-Stokes equation within a control volume as,

$$\begin{aligned} F(t) = \ & -\frac{d}{dt}\rho \int_V \mathbf{u} dV - \rho \int_S \mathbf{u}(\mathbf{u}\cdot\mathbf{n}) dS + \int_S (-p\mathbf{n} + \tau \cdot \mathbf{n}) dS \\ & -\rho \int_V \boldsymbol{\Omega} \times (\boldsymbol{\Omega} \times \mathbf{r}_{\text{pv}}) dV - \rho \int_V 2\ \boldsymbol{\Omega} \times \mathbf{u} dV - \rho \int_V \frac{d\boldsymbol{\Omega}}{dt} \times \mathbf{r}_{\text{pv}}\ dV \end{aligned} \qquad (4)$$

The sectional loads are evaluated by thin sectional control volumes with dimensions matching the field of view in the *x,y*-directions and a spanwise thickness of *dz* in the *z*-direction that is centered at a given spanwise plane. More details about the experimental & numerical setup can be found in van de Meerendonk et al. (2016).

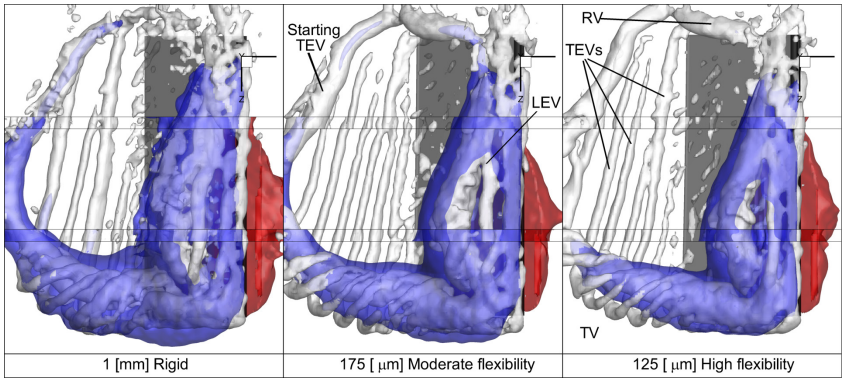

Fig. 2 Vortical structures and reconstructed pressure fields for $\delta^* = 1.5$, corresponding to a phase (rotation) angle of 36.7 deg. *Left* to *right*: rigid, moderate flexible and high flexible wing. Isosurfaces of Q-criterion in white ($Q/(V_t/c)^2 = 3$). Isosurfaces of reconstructed pressure field in blue p = -13 Pa and red p = 6 Pa (relative to ambient pressure).

RESULTS

The evolution of major vortical structures including leading edge (LEV), starting & small-scale shed trailing edge (TEV), tip (TV) and root vortices (RV) at are clearly revealed at $\delta^* = 1.5$ (see Fig 2). The spatial gradient of pressure can be related to the material acceleration in the inertial reference frame for an incompressible flow with negligible viscous effects (see Equation 2). At $\delta^* = 4$ approximate steady-state conditions are reached. The corresponding reconstructed pressure field and pressure gradient in *x*-direction are given in Figure 3. The temporal evolution of the measured and reconstructed lift and drag are compared, and the sectional lift and drag distribution at $\delta^* = 4$ are given in Figure 4.

DISCUSSION

The flow fields and fluid-dynamic loads generated by revolving low-aspect-ratio flat-plate wings with different degree of chordwise flexibility are experimentally studied using tomographic PIV and simultaneous force measurements. At low Reynolds numbers the flow field is highly repeatable, notably for the initial development phase of the flow considered in the present experiments, which allows obtaining temporal information from phase-locked measurements. The pressure field and loads have been reconstructed successfully from ensemble averaged phase-locked tomographic PIV measurements for different flexible wings, employing the non-inertial moving reference frame of the rotating wing. Furthermore, the pressure field that covers a complete wing has been successfully reconstructed from three volumes that have been measured independently, which allowed a proper comparison of pressure fields between different wings.

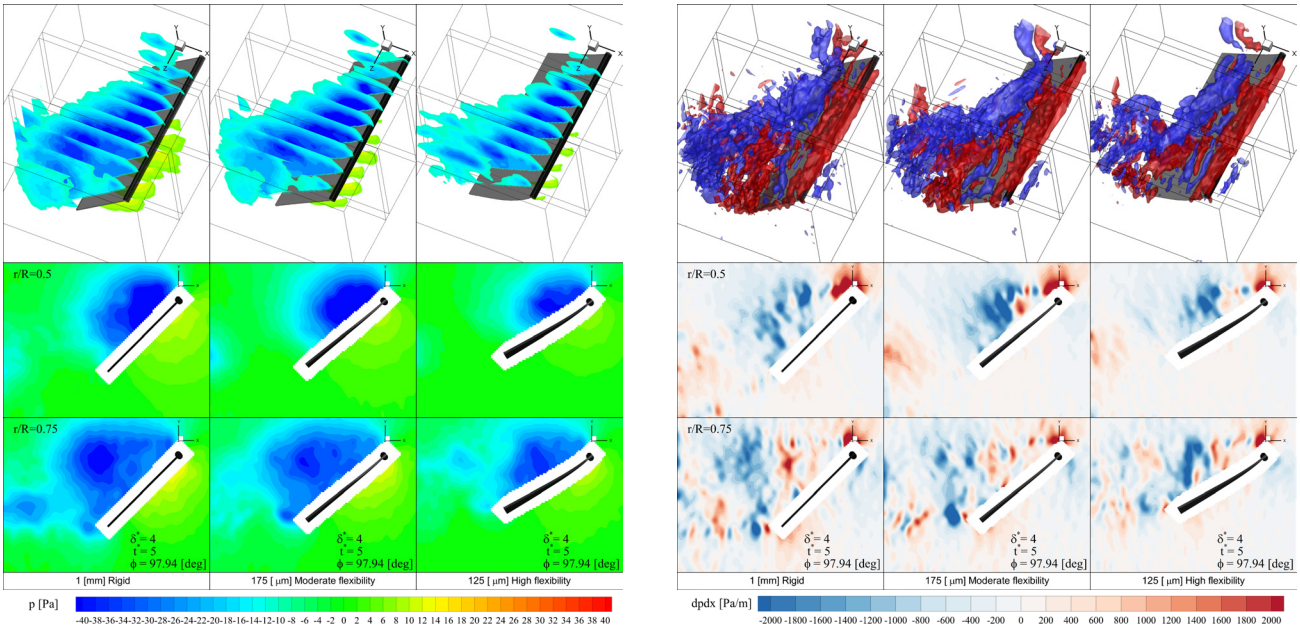

Fig. 3 *Left:* Pressure contours (*p*) at $\delta^* = 4$. *Right:* Pressure gradient in *x*-direction (*dp*/dx) at $\delta^* = 4$. Top: Along the span. *Middle:* Contour at $r/R = 0.5$. *Bottom:* Contour at $r/R = 0.75$.

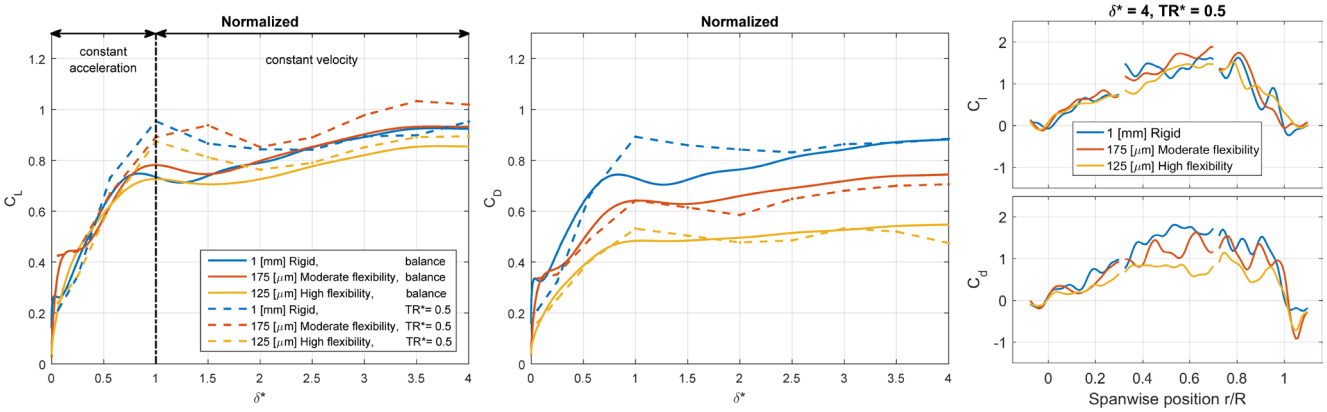

Fig. 4 *Left:* Temporal of the normalized lift (left column) and drag (right column). The reconstructed lift and drag coefficients are based on the summation of volume 1-3. The lift and drag between the different wings are normalized such that the balance and reconstructed loads match for the rigid wings at steady-state conditions. *Right:* Sectional lift and drag distribution at $\delta^* = 4$ with a temporal resolution of TR* = 0.5. The sectional control volumes have a spanwise thickness of $dz = 7$ vectors and an overlap of 6 vectors.

The vortex system structures encompass a low pressure region which has a high correlation with the vortical structures identified by the Q-criterion. As a result a comparative assessment between the different wings regarding the size of the low pressure zone associated to the LEV as well as the size of the wake can be made on the basis of the Q-criterion.

The pressure gradient information provides greater insights in the stability mechanisms of the LEV. The large regions of negative pressure gradient in *x*-direction have a high correlation with the location of the LEV. Due to these significant regions of negative pressure gradient, the particles within the LEV experience a net acceleration in the positive *x*-direction. This ensures that the LEV and its associated low pressure region is located close to the wing surface resulting in a high resultant force acting on the wing.

The normalized temporal evolution of the measured lift and drag compare reasonably well with the reconstructed lift and drag. This means that the relative differences between the wings are predicted relatively well with the load reconstruction. The sectional lift and drag provides greater insights into the distributed load mechanisms along the wing span.

REFERENCES

Birch JM (2004) Force production and flow structure of the leading edge vortex on flapping wings at high and low Reynolds numbers. Journal of Experimental Biology 207(7):1063–1072.

Combes SA, TL Daniel (2003) Flexural stiffness in insect wings I. Scaling and the influence of wing venation. Journal of Experimental Biology 206(17):2979–2987.

Ellington CP, van den Berg C, Willmott AP, Thomas ALR (1996) Leading-edge vortices in insect flight. Nature 384(6610):626–630.

Jardin T, David L (2014) Spanwise gradients in flow speed help stabilize leading-edge vortices on revolving wings. Physical Review E 90(1):013011.

Jardin T, David L (2015) Coriolis effects enhance lift on revolving wings. Physical Review E 91(3):031001.

Lentink D, Dickinson MH (2009) Rotational accelerations stabilize leading edge vortices on revolving fly wings. Journal of Experimental Biology 212(16):2705–2719.

Usherwood JR, Ellington CP (2002) The aerodynamics of revolving wings I. Model hawkmoth wings. The Journal of Experimental Biology 205(11):1547–64.

Sane SP (2003) The aerodynamics of insect flight. Journal of Experimental Biology 206(23):4191–4208.

Shyy W, Aono H, Chimakurthi SK, Trizila P, Kang CK, Cesnik CES, Liu H (2010) Recent progress in flapping wing aerodynamics and aeroelasticity. Progress in Aerospace Sciences 46(7):284–327.

van de Meerendonk R, Percin M, van Oudheusden BW (2016) Three-dimensional flow and load characteristics of flexible revolving wings at low Reynolds number. In International Symposia on Applications of Laser and Imaging Techniques to Fluid Mecahanics, number July, Lisbon.